18

SYNAPTIC INPUT TO A PASSIVE TREE

Now that we have quantified the behavior of the cell in response to current pulses and current steps as delivered by the physiologist's microelectrode, let us study the behavior of the cell responding to a more physiological input. For instance, a visual stimulus in the environment will activate cells in the retina and its target, neurons in the lateral geniculate nucleus. These, in turn, make on the order of 50 excitatory synapses onto the apical tree of a layer 5 pyramidal cell in primary visual cortex such as the one we use throughout the book, and about 100–150 synapses onto a layer 4 spiny stellate cell (Peters and Payne, 1993; Ahmed et al., 1994, 1996; Peters, Payne, and Rudd, 1994). All of these synapses will be triggered within a fraction of a millisecond (Alonso, Usrey, and Reid, 1996). Thus, any sensory input to a neuron is likely to activate on the order of 10^2 synapses, rather than one or two very specific synapses as envisioned in Chap. 5 in the discussion of synaptic AND-NOT logic.

This chapter will reexamine the effect of synaptic input to a realistic dendritic tree. We will commence by considering a single synaptic input as a sort of baseline condition. This represents a rather artificial condition; but because the excitatory postsynaptic potential and current at the soma are frequently experimentally recorded and provide important insights into the situation prevailing in the presence of massive synaptic input, we will discuss them in detail. Next we will treat the case of many temporally dispersed synaptic inputs to a leaky integrate-and-fire model and to the passive dendritic tree of the pyramidal cell. In particular, we are interested in uncovering the exact relationship between the temporal input jitter and the output jitter.

The bulk of this chapter deals with the effect of massive synaptic input onto the firing behavior of the cell, by making use of the convenient fiction that the detailed temporal arrangement of action potentials is irrelevant for neuronal information processing. This allows us to derive an analytical expression relating the synaptic input to the somatic current and ultimately to the output frequency of the cell. Under these conditions, continuous input variables—the firing rates of the presynaptic neurons—are mapped onto a continuous output frequency.

18.1 Action of a Single Synaptic Input

In general, it is very difficult to quantify the effect that an individual synapse has on the potential at the soma or on the firing frequency of the cell using a single measure. The reason is, of course, that synaptic input needs to be treated as a time-varying conductance change somewhere in the dendritic tree acting upon a nonlinear and nonstationary system. In neural network models, this is quite a different manner, since the complexity of synapses is reduced to a scalar weight w_{ij}, all synaptic input arrives at a single compartment, and the spiking nonlinearity is a stationary one (Chap. 14).

18.1.1 Unitary Excitatory Postsynaptic Potentials and Currents

Figure 18.1 illustrates the local and somatic EPSPs in response to a single excitatory, voltage-independent synapse at one of three different locations in the tree (apical and basal dendrite and the soma; see Fig. 18.6). The resultant EPSP is sometimes also called *unitary* EPSP. We include the situation of an excitatory synapse at the soma—even though no or only very few excitatory synapses are located at the cell body of pyramidal neurons—because it represents a sort of baseline against which the other cases can be judged. Furthermore, a significant fraction of excitatory synapses on smooth, that is, inhibitory, interneurons is made onto or close to the soma.

The local EPSPs peak within 1–1.2 msec, gradually returning to the resting potential with a time course dictated by τ_m. The somatic EPSPs undershoot V_{rest} before returning to base levels. This small hyperpolarizing response is caused by activation of two potassium

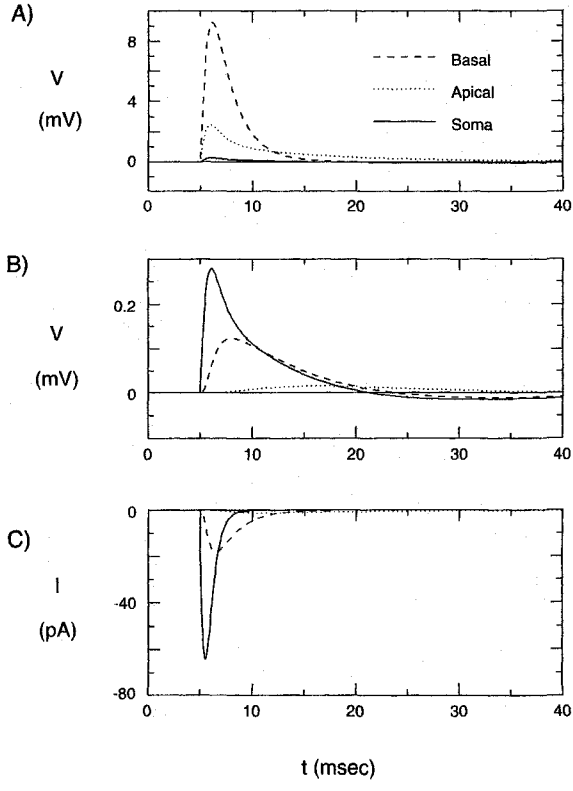

Fig. 18.1 VOLTAGE-INDEPENDENT UNITARY SYNAPTIC INPUT Excitatory postsynaptic potential (EPSP) at the site of the synapse **(A)** and at the soma **(B)**. A single fast AMPA synapse ($g_{\text{peak}} = 1$ nS; $t_{\text{peak}} = 0.5$ msec) was either located in the apical tree (arrow in Fig. 18.6; dotted line), toward the end of a basal dendrite (arrow in Fig. 18.6; dashed line), or at the soma (solid line). The undershoot in the somatic EPSPs is caused by activation of potassium currents. **(C)** Excitatory postsynaptic current (EPSC) at the soma for the same three synaptic inputs while the membrane potential at the soma is clamped to V_{rest}. The resulting current flows inward, plotted negative by convention, and peaks prior to the peak in the associated somatic EPSP.

currents I_A and I_M. Phenomenologically, the undershoot arises from the linear but inductive nature of the potassium currents for small voltage excursions around rest (Sec. 10.1 and Fig. 10.5).

Figure 18.1 also depicts I_{clamp} in response to the three synaptic inputs when the somatic potential is clamped to $V_{rest} = -65$ mV. The peak current varies fiftyfold, from -1.2 pA for the distal apical input to -64 pA for the somatic one. The somatic EPSCs peak earlier than the associated somatic EPSPs, compatible with the notion that the current leads the voltage expected of an RLC circuit dominated by the resistive and capacitive components.

Note that the EPSC does *not* correspond to the current flowing during the somatic EPSP, since in the former case the somatic potential is clamped (explaining the lack of a positive, outward current during the late phases of the EPSC). The actual current flowing across the membrane during the EPSP will show such an outward component due to the hyperpolarizing swing of the membrane potential. Yet, because the membrane potential during the EPSP does not deviate much from V_{rest} under the conditions extant in Fig. 18.1, the EPSC is qualitatively similar to the current flowing during the EPSP.

Activating a single synapse whose conductance is halfway split between voltage independent AMPA receptors and voltage-dependent NMDA receptors perturbs this picture but little. Its primary effect is to prolong the duration of the EPSP and the EPSC. The reason for the discrepancy between the small effect of voltage-dependent input in the situation considered here and the much larger effect apparent in the experiment of Stern, Edwards, and Sakmann (1992) pictured in Fig. 4.9 is that in the former the local EPSP barely reaches 8 mV, an insufficient depolarization to remove the magnesium blockage of the NMDA receptor channels. Thus, blocking the NMDA component (as in Fig. 4.9B) has little effect. In the experiment, focal stimulation recruited a much larger number of synapses which locally depolarized the membrane sufficiently to activate NMDA input.

How do these simulated EPSPs and EPSCs stack up against experimental data from layer 5 pyramidal cells in the rat visual cortex? Figure 18.2 histograms the time course and the peak amplitudes of about 1000 spontaneous EPSCs (clamped around the resting potential) and close to 500 spontaneous EPSPs (from the monumental efforts of Smetters, 1995).

The time courses of experimentally recorded somatic EPSPs and EPSCs are comparable to those of Fig. 18.1, compatible with a very fast ($t_{peak} = 0.5$ msec), AMPA-mediated conductance change and a slow membrane time constant. The amplitude histograms of the EPSCs encompass the three simulated values from Fig. 18.1C. (The locations of the synapses that gave rise to the data in Fig. 18.2 are not known, but are assumed to be distributed throughout the dendritic tree.) The somatic EPSPs are, however, much larger than the simulated ones, due to a mismatch in input impedances in the two cases. This is expected, since the simulated pyramidal cell receives 2 Hz synaptic background activity, which substantially lowers the input impedance everywhere (see the following section).

Close inspection of Fig. 18.2 reveals a systematic dependency of the rise time of the EPSPs with their width. Rall (1967; Rall et al., 1967) first derived the relationship expected between the rise time of a unitary EPSP and its halfwidth; for more distant input, the rise time of the somatic EPSP will be longer and it will be more spread out. Plotting these two measures of dispersion against each other, known as a *shape index plot* (Rall et al., 1967), can reveal something about the distance between the synapse and the soma. As applied to spinal motoneurons, these techniques played an important role in establishing the importance of dendritic location (Redman and Walmsley, 1983).

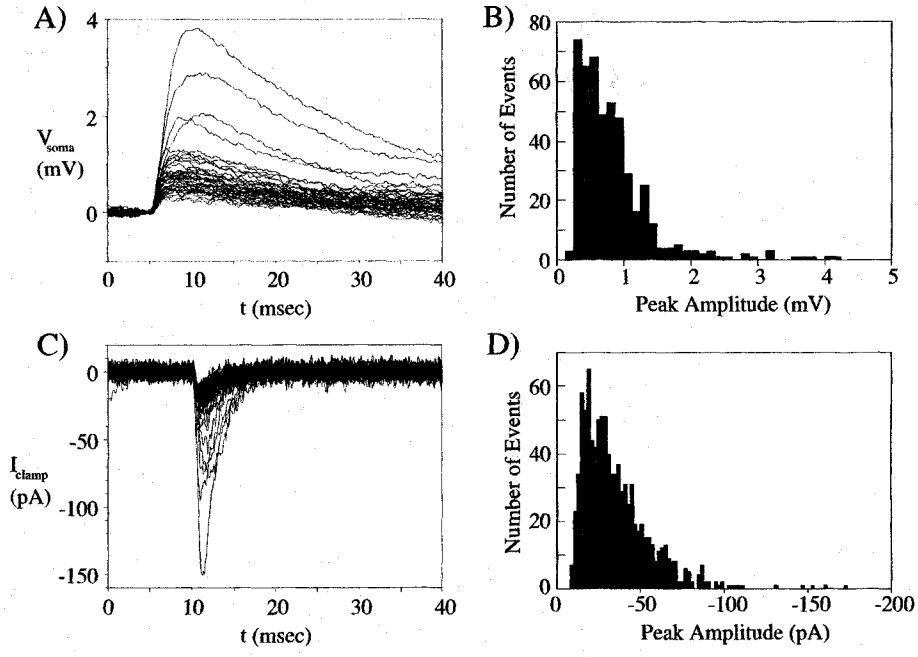

Fig. 18.2 Experimentally Recorded Unitary EPSPs and EPSCs Spontaneous **(A)** EPSPs and **(C)** EPSCs recorded from layer 5 pyramidal cells in slices of rat visual cortex in the presence of bicuculline to block synaptic inhibition. The histograms of **(B)** the peak amplitude of the EPSPs (n = 479) and **(D)** the EPSCs (n = 953) reveal a broad distribution, due to the fact that the synaptic origins of the observed events are distributed throughout the dendritic tree. Reprinted by permission from Smetters (1995).

18.1.2 Utility of Measures of Synaptic Efficacy

As discussed extensively in Sec. 3.2, Rall (1962, 1964) showed that under certain conditions a dendritic tree can be reduced to a single finite cable, the *equivalent cylinder*. In particular, at each branch point the $d^{3/2}$ law, governing the relationship between parent and daughter branches, must hold and all dendrites must terminate at the same electrical distance from the soma. Unfortunately though, dendritic branch points of pyramidal cells, according to Larkman et al., (1992; see also Hillman, 1979; Brown, Fricke, and Perkel, 1981; Johnston, 1981) do not obey the $d^{3/2}$ law. Furthermore, the apical tree is electrically much longer than the basal dendrites, violating another condition needed to reduce the cell to a single cylinder.

In Sec. 3.5, we introduced several measures of synaptic "efficiency," such as the electrotonic distance between a site i and the soma L_{is} (a cumulative measure of the normalized electrotonic distance between i and the soma) and the logarithm of the voltage attenuation L_{is}^{v} (Eq. 3.38). Recall that in an infinite cable, $L = L^{v}$. In Table 18.1 these factors are evaluated for the apical and basal synaptic input of Fig. 18.1, where $L_{is}^{v,t}$ is the logarithm of the actual voltage attenuation experienced by the synaptic input. (L_{is}^{v} is computed from the dc input and transfer resistances as in Eq. 3.38.) Because the dendritic tree cannot be approximated by an equivalent cable but has pronounced asymmetries—current flows much more easily toward than away from the soma—the electrotonic distance L is

pretty much useless as a quantitative indicator for attenuation. The log attenuation predicted by the stationary input and transfer resistances does a much better job, coming within 14% of the true log attenuation. This difference is, of course, due to the transient nature of the synaptic input.

The discrepancies between the actual attenuation of the EPSPs and the attenuation predicted by the electrotonic length apparent in Table 18.1 provide a convincing numerical argument *against* using the electrotonic distance L—derived from solving the linear cable equation in finite cables—as a measure of the coupling of a synapse to the soma.

18.1.3 What Do Unitary EPSPs and EPSCs Tell Us about the Threshold?

As we learned in the previous chapter, the pyramidal cell model possesses a voltage threshold V_{th} (around −49 mV) for rapid synaptic input. We should therefore be able to estimate the number of simultaneously excitatory synaptic inputs needed to reach threshold n_{th} as the effective threshold voltage, $V_{\text{th}} - V_{\text{rest}} = 16$ mV, divided by the peak unitary somatic EPSP amplitude. For an excitatory input at the soma, $V_{\text{peak}} = 0.28$ mV (solid trace in Fig. 18.1), leading to $n_{\text{th}} = 57$. From numerical simulations, we know that the actual number is $n_{\text{th}} = 64$. This estimate does not take the changing driving potential into account. (At −65 mV, the driving potential for the synaptic input is 16 mV larger than at threshold.)

The effect of synaptic saturation (Fig. 4.11) at high-impedance sites, such as the distal, apical, or the basal tree, complicates this simple analysis. Many distal sites are prevented from generating sufficiently large somatic EPSPs to ever reach threshold. At the soma, the input (slope) conductance of 60.6 nS is large enough compared to the peak conductance change of a single synapse (0.5 nS) for saturation not to play a role. Furthermore all voltage-dependent currents but sodium activation can be considered to be stationary, thereby approximating the conditions under which V_{th} was estimated. We conclude that the unitary EPSP amplitude can be used to predict the voltage threshold remarkably well (see also Koch, Bernander, and Douglas, 1995).

Applying the same logic to estimate I_{th} predicts that nine such somatic inputs, each delivering 33 pA (Fig. 18.1C), suffice to reach I_{th}, underestimating the actual number by a factor of 7. But, as we pointed out in Sec. 17.3.4, the concept of a current threshold is only applicable for sustained inputs. The highly transient EPSCs cannot be used to estimate the threshold. (This was illustrated in Fig. 17.5A, in which the total synaptic current flowing onto the spike initiating membrane I_{soma} exceeds I_{th} numerous times without initiating a spike.)

We conclude that when considering rapid synaptic input, the somatic potential due to synaptic activity is a more relevant variable than the current obtained under voltage clamp for predicting when the cell will trigger an action potential.

TABLE 18.1
Voltage Attenuation of Synaptic Input

Position	$\tilde{K}_{ii}$	$\tilde{K}_{is}$	$\tilde{K}_{ss}$	L	L_{is}^{v}	$L_{is}^{v,t}$
Basal	387.79	18.47	16.48	0.24	3.32	4.32
Apical	341.68	10.47	16.48	0.56	3.48	5.07

Actual and expected voltage attenuation between the two synaptic sites used in Fig. 18.1 and the soma as computed from the stationary input ($\tilde{K}_{ii}$ in MΩ) and transfer resistance ($\tilde{K}_{is}$ in MΩ). $e^{L_{is}}$ is the attenuation expected from the electrotonic length measurement (Eq. 3.33); L_{is}^{v} is defined via Eq. 3.38 as the logarithm of the voltage attenuation. In an infinite cable $L = L^{v}$. Due to the pronounced asymmetries in the cable structure, these two measures here differ markedly. The natural logarithm of the actual voltage attenuation $L_{is}^{v,t}$, as defined by the peak EPSP values in Fig. 18.1, is larger than L_{is}^{v} due to the distributed capacitances that preferentially remove high temporal frequencies (in particular for the distal, apical input).

18.2 Massive Synaptic Input

Now that we have seen the effect of a single synapse, we are ready to deal with the much more physiological situation in which a hundred or more synapses are simultaneously activated. How will this affect the somatic potential and current and, ultimately, the firing frequency of the cell? Because of the nonlinear relationship between synaptically induced conductance changes and the membrane potential, this question is not easy to answer in general. Let us start by studying the situation when the neuron is bombarded with numerous individual excitatory and inhibitory inputs.

18.2.1 Relationship between Synaptic Input and Spike Output Jitter

When a cortical neuron is presented with the appropriate stimulus, it rapidly and reliably increases its probability of firing. Individual cortical neurons respond to a dynamic random dot motion stimulus with a highly reproducible temporal modulation of their firing rate, precise to a few milliseconds (Fig. 15.11). The time that it takes for such a cell to significantly modulate its firing rate—as determined by averaging over many presentations of an identical stimulus—is almost always less than 10 msec and occurs in neurons that are at least six synapses removed from the periphery. This precision is surprising because the propagation of an input through a multilayer network with continuous mean rates causes rise times to become increasingly shallow (due to the low-pass filtering effect treated in Sec. 14.2.4).

Yet, as the sensory triggered "wave" of activity propagates through many layers of the cortex, the signal does not appear to become appreciably rounded off, but is only delayed between consecutive stages by about 10 msec. This has been assessed directly by comparing the latency and rise time of neurons in different cortical areas to the same stimulus. In the case of an awake monkey, neurons in the primary visual cortex responded to a visual stimulus with an average 10–90% rise time of 8 msec while neurons in a subsequent processing stage, cortical area V4, show a virtually identical rise time of 7 msec but with an additional 26 msec latency (Marsalek, Koch, and Maunsell, 1997).

Let us address this important problem in the following manner. Suppose an instantaneous sensory event in the world triggers a volley of activity in n excitatory synaptic inputs. We will assume that the arrival time of the input is centered around $t = 0$ and that its standard deviation in time, here called input jitter, is σ_{in}. If we further suppose that these n synapses are sufficient to trigger one (or more) spikes (that is, $n > n_{\text{th}}$) we can compute the standard deviation in time, termed the output jitter σ_{out}, of the spike triggered in response to this input. This will help us understand to what extent temporal jitter in the input is preserved, amplified, or reduced by multiple processing stages.

We first deal with a simplified problem by assuming that the probability density of the arriving synaptic inputs $p_{\text{in}}(t)$ is the uniform density on the interval [0,1]. ($p_{\text{in}}(t) = 1$ for $t \in [0, 1]$, and 0 otherwise.) Different from before, we assume that each input only triggers a single synaptic event of postsynaptic strength a_e. These inputs are integrated onto the capacitance of a nonleaky integrate-and-fire unit (of voltage threshold $V_{\text{th}} = a_e n_{\text{th}}$). Together with the uniform density, this assures us that at t = 1 the voltage will be exactly na_e (in the absence of a threshold).

The probability that the voltage at time t has attained the value $n_{\text{th}} a_e$ is given by the *beta density* (Papoulis, 1984)

$$p_{\text{out}}(t) = \frac{(n+1)!}{n_{\text{th}}!\,(n-n_{\text{th}})!} t^{n_{\text{th}}} (1-t)^{(n-n_{\text{th}})}. \tag{18.1}$$

The standard deviation of this distribution is

$$\sigma = \sqrt{\frac{(n_{\text{th}} + 1)(n + 1 - n_{\text{th}})}{(n + 2)^2(n + 3)}}. \tag{18.2}$$

In the case of the uniform probability density, $\sigma_{\text{in}} = 1/2\sqrt{3}$, allowing us to rescale Eq. 18.2 in terms of the output jitter,

$$\sigma_{\text{out}} = \sigma_{\text{in}} 2\sqrt{3} \sqrt{\frac{(n_{\text{th}} + 1)(n + 1 - n_{\text{th}})}{(n + 2)^2(n + 3)}}. \tag{18.3}$$

What happens if the number of synaptic inputs n greatly exceeds the number of inputs required to bring the cell to fire n_{th}? Making the approximations that $n + 3 \approx n + 2 \approx n$, that $n + 1 - n_{\text{th}} \approx n$, and $n_{\text{th}} + 1 \approx n_{\text{th}}$, we arrive at

$$\sigma_{\text{out}} \approx \sigma_{\text{in}} 2\sqrt{3} \frac{1}{n} \sqrt{\frac{V_{\text{th}}}{a_e}}. \tag{18.4}$$

Or, the output jitter is inversely proportional to the number of excitatory synaptic inputs. This makes sense, since the time it takes to reach threshold will be proportional to the drift that is dictated by n. The jitter in the time to threshold is inversely related to the drift. Of course, our derivation only holds under conditions when the membrane leak can be neglected (that is, when most of the synaptic input arrives within a fraction of τ).

Detailed simulations using a leaky integrate-and-fire model as well as our customary layer 5 pyramidal cell compartmental model bear this out (Fig. 18.3A; for the details, consult Marsalek, Koch, and Maunsell, 1997). In the presence of massive excitatory input ($n = 250$, with $n_{\text{th}} = 66$; see previous section), whose arrival time has a Gaussian distribution in time, the relationship between σ_{in} and σ_{out} is a linear one, with a slope of around 0.116, as expected from the approximation in Eq. 18.4. Adding inhibitory synaptic input increases this slope, but not substantially (Fig. 18.3B). Any more inhibition and the cell fails to reach threshold in a growing fraction of all trials.

In the case of massive synaptic input, the temporal output jitter will be smaller than the input jitter. It follows that for a cascade of spiking cells, the output jitter converges to zero (Marsalek, Koch, and Maunsell, 1997; see also Abeles et al., 1994; Hermann, Hertz, and Prügel-Bennett, 1995). In real networks the jitter is unlikely to become vanishingly small since we neglect several additional sources of timing variability. The two most dominant sources are likely to be:

1. The inhomogeneous spike propagation times between consecutive layers of neurons due to variations in the diameter and length of the associated axons and axonal terminations (wiring jitter). We considered these axonal delays in Fig. 6.17 and found that they are small (on the order of ± 0.5 msec).

2. Jitter in the delay between presynaptic spikes and the opening of the postsynaptic synaptic channels (synaptic jitter).

We conclude that the output jitter in a network with many layers of spiking neurons (such as in Abeles's (1990) synfire-chain model) converges to a fixed but small number, bounded by the "jitter" in the anatomical connections and in the synaptic transduction process.

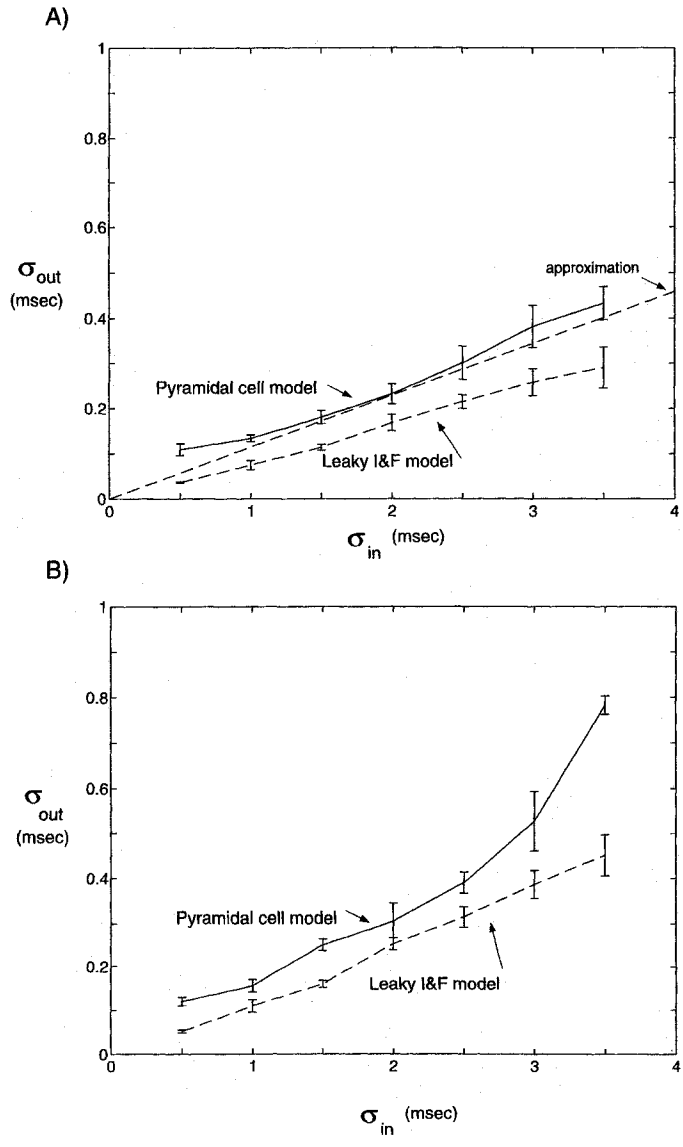

Fig. 18.3 Relationship between Input and Output Jitter What is the relationship between the standard deviation in time of synaptic input σ_{in} and the standard deviation in time of the resultant output spike σ_{out}? Marsalek, Koch, and Maunsell (1997) treated this question using a leaky integrate-and-fire model and the more complex layer 5 pyramidal cell compartmental model. **(A)** 250 excitatory fast voltage-independent synaptic inputs are triggered once. The probability density function $p_{in}(t)$ is Gaussian with standard deviation σ_{in}. For the integrate-and-fire model, synapses are assumed to be linear current sources, with $a_e = 0.23$ mV; $\tau = 10$ msec. For the compartmental model, synapses are of the fast AMPA type, distributed throughout the dendritic tree. In both cases, the effective voltage threshold $V_{th} = 16$ mV and $n_{th} = 66$. Equation 18.4 predicts a linear relationship between σ_{in} and σ_{out} with slope 0.116 (line labeled "approximation"). Error bars correspond to the standard deviation from five runs with 50 spikes each. **(B)** A qualitatively similar result is obtained if 62 inhibitory synapses are added (hyperpolarizing current synapses with $a_i = 0.23$ mV for the integrator and $GABA_A$ synapses for the more detailed model). Any more inhibition, and the cell frequently fails to trigger a spike. Thus, a spiking cell with a passive dendritic tree can reduce input jitter provided that n is much bigger than n_{th}. Reprinted by permission from Marsalek, Koch, and Maunsell (1997).

18.2.2 Cable Theory for Massive Synaptic Input

Standard one-dimensional passive cable theory (Jack, Noble, and Tsien, 1975; Rall, 1989) assumes that the electrotonic structure of the cell does not change in response to synaptic input. As long as synaptic input is treated as a de- or hyperpolarizing current this is certainly true. The independence of the electrical structure from the input allows us to characterize the spatio-temporal integrative properties of the cable or the cell in terms of the transfer and input impedances as well as space and time constants.

Yet as we emphasized from the beginning of this book, even the activity of a single synapse has an impact on the input impedance $K_{ii}(t)$ (e.g., Eq. 4.24). While the actual size of this effect is negligible for one or a few isolated synaptic inputs, it can dominate the behavior of the system for large inputs. This is particularly true given that patch-clamp recordings of pyramidal and Purkinje cells find very high values for the passive membrane resistance (on the order of 100,000 $\Omega \cdot cm^2$; see Appendix A).

Let us exemplify our argument with some numbers. Assume a small, spherical cell with a radius equal to $r = 15\ \mu m$. Its input conductance $G_{in} = 4\pi r^2 / R_m$ amounts to only 0.28 nS and its time constant to 100 msec for $R_m = 100,000\ \Omega \cdot cm^2$. Activation of a single synapse with $g_{peak} = 0.5$ nS will immediately, albeit briefly, triple the effective input conductance and reduce the time constant to a third of its original value. A second synapse will not find the same electrotonic structure present as the first one did. It is immaterial for this argument whether the synapse considered is excitatory or inhibitory, as long as it increases the local membrane conductance. The fact that synaptic inputs can significantly affect the electrotonic structure of the cell depends on the fact that R_m is high relative to the inverse of the synaptic-induced conductance change. For low values of R_m, say in the neighborhood of 2,000 $\Omega \cdot cm^2$, many more synaptic inputs would have to be activated in order for the synaptic conductance to dominate the conductance contributed by the passive membrane of the cell.

As expressed in a perfunctory manner in Sec. 4.9.1, Eq. 4.24 describes the dependency of $K_{ii}(t)$ on the exact timing of the synaptic input $g_{syn}(t)$. Clearly, for two or more synapses, the dependency can be considerably more complex, since the input impedance and other cable properties also depend on the relative timing between the inputs and whether or not they are correlated.

In order to study the effect of massive synaptic input on the cell, we will disregard such temporal effects by assuming that the inputs arriving at different synapses are independent of each other and replace the series of presynaptic spikes by an instantaneous rate f_i. We also disregard any detailed dynamics of the spiking by a "suitable" temporal averaging procedure that reduces the total synaptic input from n independent synapses to any one particular compartment to a single number,

$$\overline{g} = \sum_{i=0}^{n} \overline{g_i}\, \langle f_i \rangle \tag{18.5}$$

where $\overline{g_i}$ represents the integrated conductance for a single input,

$$\overline{g_i} = \int_0^{+\infty} g_i(t)dt\,. \tag{18.6}$$

When $g_i(t)$ has the form of an α function (Eq. 4.5), $\overline{g_i} = e g_{peak} t_{peak}$. If the synapse is of the NMDA type, this average conductance will be voltage dependent, rendering the following equations slightly more complex. Obviously, this averaging method does not incorporate any short-term synaptic changes observed in brain slices (Sec. 13.5.4), such as short-term depression and facilitation.

With this averaging procedure in place, we can replace the different types of synapses in each compartment (AMPA, NMDA, $GABA_A$, and so on) as well as the leak conductance by a single "effective" conductance,

$$G_{\text{eff}} = \sum_{i=1}^{n} \overline{g_i} \langle f_i \rangle + G_m A \tag{18.7}$$

in series with a single effective battery,

$$E_{\text{eff}} = \frac{\sum_{i=1}^{n} E_i \overline{g_i} \langle f_i \rangle + E_{\text{leak}} G_m A}{G_{\text{eff}}} \tag{18.8}$$

where A is the membrane area of the compartment needed to convert the leak conductance per unit area, G_m, into an absolute conductance. Equation 18.7 tells us that as the presynaptic firing frequency $\langle f_i \rangle$ increases, so does the postsynaptic membrane conductance, regardless of whether the synapses are excitatory or inhibitory. Only the conglomerate reversal potential E_{eff} is influenced by the signs and amplitudes E_i of the synaptic batteries: if inhibitory cells fire more strongly than excitatory ones, the effective synaptic reversal potential will be pulled toward more hyperpolarizing values and *vice versa*. We conclude that the effective membrane resistance should not be thought of as a fixed parameter, but as a dynamic variable that can change within a fraction of a second, in contrast to the intracellular resistivity and the membrane capacity, which appear much more difficult to modulate rapidly.

For a single infinite cylinder with the appropriate boundary condition, we can write down a slightly modified cable equation,

$$\frac{d}{4R_i G_{\text{eff}}} \frac{\partial^2 V_m(x,t)}{\partial x^2} = \frac{C_m}{G_{\text{eff}}} \frac{\partial V_m(x,t)}{\partial t} + (V_m(x,t) - E_{\text{eff}}) \tag{18.9}$$

which contains a single term accounting for all synaptic conductances. Defining the length constant of the cable (Eq. 2.13) as

$$\lambda = \sqrt{\frac{d}{4R_i G_{\text{eff}}}} \tag{18.10}$$

and the time constant as

$$\tau_m = \frac{C_m}{G_{\text{eff}}} \tag{18.11}$$

we arrive back at the standard normalized cable equation (Eq. 2.7),

$$\lambda^2 \frac{\partial^2 V_m(x,t)}{\partial x^2} = \tau \frac{\partial V_m(x,t)}{\partial t} + (V_m(x,t) - E_{\text{eff}}) . \tag{18.12}$$

In the remainder of this chapter, we will deal with three distinct scenarios of time-averaged massive synaptic input. We start off by analyzing the effect of diffuse synaptic activity that occurs throughout the cell before we turn toward an analysis of the effect of massive excitatory and shunting inhibitory synaptic activity on the cell.

18.3 Effect of Synaptic Background Activity

Neurons, just like people, do not exist in isolation but are embedded within a tightly interwoven network of other nerve cells. A typical neocortical pyramidal cell is the recipient of anywhere between 5000 and 20,000 synapses from other neurons, while Purkinje cells

in the cerebellum may receive up to 200,000 synapses. In the lightly anesthetized animal as well as in the awake behaving animal, these cells are "spontaneously" active, which means in practice that they generate action potentials that cannot readily be accounted for by the presence of any simple sensory stimulus (such as a bright bar or a loud tone). The origin of this spontaneous activity is presently unknown but could be due to several sources: (1) the remnants of spontaneous activity at the sensory periphery that has percolated to the more central stages (e.g., photon shot noise in the photoreceptors), (2) the spontaneous spiking due to channel fluctuations (Sec. 8.3.2), or (3) the spontaneous release of synaptic vesicles in the absence of significant presynaptic activity.

Experimentally recorded values of the spontaneous firing in cortex range, from low values of 0.25–2.5 spikes per second in the anesthetized cat visual cortex (Gilbert, 1977; Leventhal and Hirsch, 1978) to larger values of 5–10 Hz in extrastriate areas, such as the cat motor cortex (Woody, Gruen, and McCarley, 1984), the rat sensory-motor cortex (Bindman and Prince, 1983), the auditory cortex in rhesus monkeys and baboon (Abeles, 1990), and the inferior temporal cortex of the behaving monkey (R. Desimone, personal communication).

These nonzero rates of background activity are in sharp contrast to the situation prevailing for brain slices or for cultured neurons. The removal of afferent fibers (by cutting to extract the slice from the brain), combined with the absence of the right combination of neuromodulators and growth factors, makes neurons rather reticent about firing in the absence of a direct electrical or pharmacological stimulus.

What consequence does this background activity, expressed via the time-averaged rate $\langle f_b \rangle$, have on any one neuron? Barrett (1975) first brought up the possibility that synaptic background activity might affect the electrical properties of α motoneurons (see also Rall, 1974). The subject remained dormant until a number of groups took up the issue via detailed compartmental simulations (Holmes and Woody, 1989; Bernander et al., 1991; Rapp, Yarom, and Segev, 1992) and analytical investigations (Abbott, 1991).

We will summarize the results of these studies by focusing on the changes in R_{in}, τ_m, L, and V_{rest} wrought by varying the background firing rate $\langle f_b \rangle$.

18.3.1 Input Resistance

The input resistance of the finite cable (looking toward the sealed end boundary at the other terminal) is specified by Eq. 2.21 as

$$R_{\text{in}} = \frac{2R_i^{1/2}}{\pi d^{3/2}} \frac{\coth(L)}{G_{\text{eff}}}, \tag{18.13}$$

where $L = \ell/\lambda$ is the electrotonic length of the cable. In the limit of an infinite high background activity, that is, for $\langle f_b \rangle \to \infty$, R_{in} decreases as $\langle f_b \rangle^{-1/2}$. Basic intuition tells us that additional synaptic input, independent of whether excitatory or inhibitory, increases the membrane conductance and thereby drives down the effective membrane resistance R_{eff} (Fig. 18.4A).

The same plot also shows R_{in} for the compartmental model of the pyramidal cell with the standard complement of voltage-dependent somatic membrane conductances ("active" neuron) and for the same model but in the absence of these active conductances ("passive" model). (The geometry of the single cylinder was adjusted to coincide with the passive pyramidal cell model at $\langle f_b \rangle = 0$.) All three models share the same features: as $\langle f_b \rangle$ is turned up from 0 to 2 Hz, the input resistance drops by a factor of 10, from 193 to 20 MΩ, in the passive case, and by a factor of 4, from 50 to 12 MΩ, in the active case. The deviation

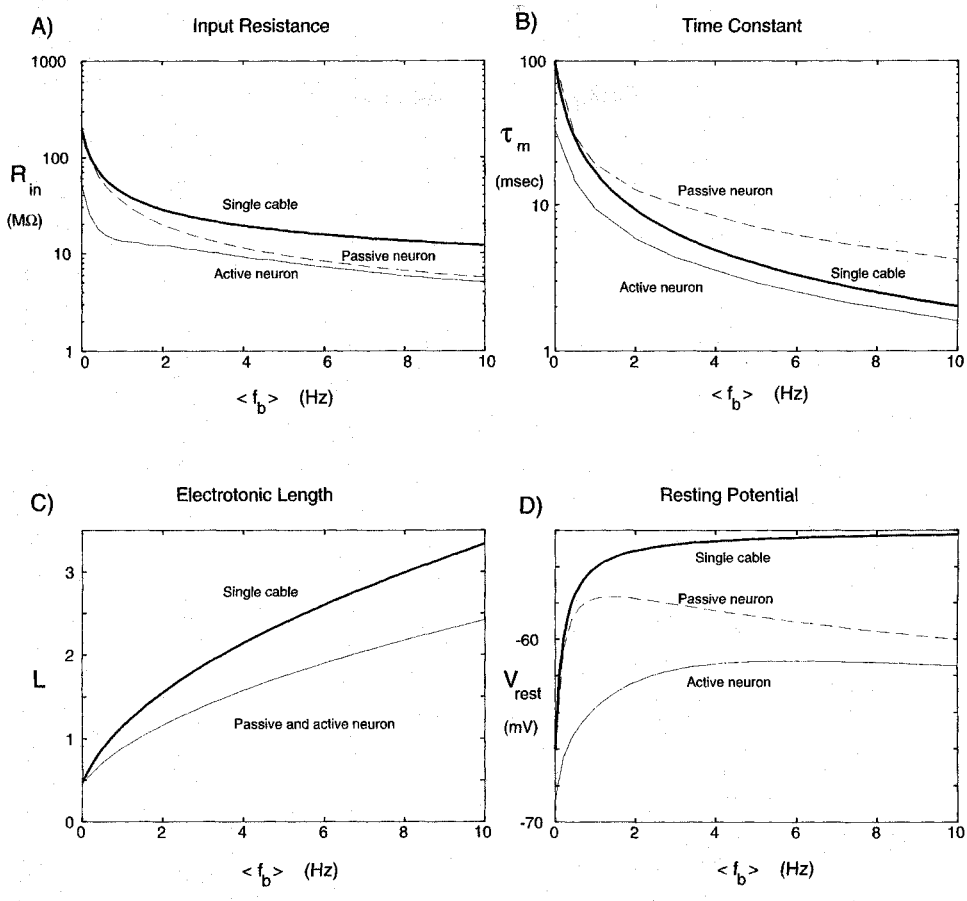

Fig. 18.4 Effect of Synaptic Background Activity on R_{in}, τ_m, L, and V_{rest} Illustration of the effect of varying the synaptic background activity $\langle f_b \rangle$ on four variables characterizing spatio-temporal integration in three systems; a finite, passive cylinder (3060 μm long and 5.8 μm thick; with sealed-end boundary condition; bold line labeled "single cable"), the complete model of the layer 5 pyramidal cell with active conductances ("active" neuron) and the same model but with all active somatic conductances removed ("passive" neuron). All cases show the same effect: as $\langle f_b \rangle$ increases, the membrane becomes more and more leaky, and R_{in} as well as τ_m decrease and the electrotonic length of the passive cable or the electrotonic distance between a point in the layer 1 portion of the distal apical tree and the soma in the pyramidal cell becomes ever larger. $\langle f_b \rangle$ is very close to zero in brain slices, while $\langle f_b \rangle > 1$ Hz corresponds to the situation in the living brain. The behavior of the cable is given by the equations in the text. R_{in}, τ_m, and V_{rest} are all measured at the soma. Inhibitory and excitatory synapses are assumed to have identical rates $\langle f_b \rangle$. Note the logarithmic scale on the upper two panels. Reprinted by permission from Bernander (1993).

of the compartmental model from the cylinder at high values of $\langle f_b \rangle$ is largely explained by the inhomogeneous synaptic distribution along the pyramidal cell (inhibitory synapses cluster in a neighborhood of the soma while excitation is more distal). Further differences result from the voltage-dependent components.

The dependency of R_{in} and other electrical parameters on $\langle f_b \rangle$ becomes more complex in the presence of voltage-dependent NMDA input. As discussed in Sec. 17.1.2 and Fig. 17.3, incorporating NMDA conductances into the membrane can have the paradoxical effect of reducing the slope conductance. For the situation discussed here, this implies that under

certain conditions the input resistance can actually increase as the background firing rate is increased (Bernander, 1993).

18.3.2 Time Constant

Equation 18.11 characterizes the dependency of the passive time constant on $\langle f_b \rangle$. We expect that as $\langle f_b \rangle \rightarrow \infty$, τ_m goes to zero as $1/\langle f_b \rangle$. The fractional decrease in the somatic time constant is similarly large in the compartmental model: from 100 to 12.8 msec for the passive case and from 33.7 to 5.9 msec in the active case (Fig. 18.4B). This decrease in τ_m as $\langle f_b \rangle$ increases implies that the pyramidal cell becomes much more sensitive to the degree of temporal dispersion in any synaptic input. To demonstrate this, Bernander and colleagues (1991) computed n_{th}, the average number of excitatory non-NMDA synapses, distributed throughout the dendritic tree, necessary to trigger a spike. These synapses were either all activated simultaneously or spread out over a 25 msec extended time window (with each synapse activated only once).

It is apparent from Fig. 18.5 that for the desynchronized case n_{th} increases significantly as $\langle f_b \rangle$ increases. Under slice conditions, 115 synchronized synapses are necessary to bring the cell above threshold, whereas 145 are needed if the input is desynchronized. This small difference between synchronized inputs and inputs arriving smeared out in time is due to the long integration period of the cell ($\tau_m = 100$ msec). For a 1 Hz background activity, 113 synchronized or 202 desynchronized inputs are needed to fire the cell. At $\langle f_b \rangle = 7$ Hz, when 35,000 synaptic events are bombarding the cell every second, 3.5 times as many

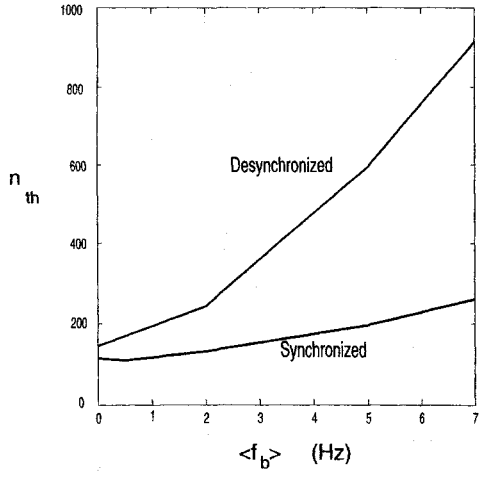

Fig. 18.5 TEMPORAL INTEGRATION The ability of the standard layer 5 pyramidal cell to distinguish coincident arriving synaptic input from a desynchronized one increases as the spontaneous background activity $\langle f_b \rangle$ increases and τ_m decreases (Fig. 18.4B). The minimal number of excitatory voltage-independent synaptic inputs n_{th} (with $g_{\text{peak}} = 0.5$ nS) needed to trigger a spike at the soma as a function of $\langle f_b \rangle$. The synapses are spread over the dendritic tree in accordance with the known distributions and are either all activated simultaneously or activated once over a 25-msec-wide window, independently of each other. For $\langle f_b \rangle \approx 0$ (a situation prevalent for most *in vitro* studies), the difference between synchronized and desynchronized inputs is minor but becomes substantial when the overall network activity is high. The average background activity can therefore be seen as the signal controlling the temporal tuning properties of the cell. Each simulation is run numerous times using a different distribution of synapses. Reprinted by permission from Bernander et al., (1991).

desynchronized inputs are needed to trigger the cell than if the inputs arrive together. As $\langle f_b \rangle$ increases, the cell becomes more and more selective to differences in the arrival times of synaptic inputs.

18.3.3 Electroanatomy

According to Eq. 18.10, the electrotonic length of a finite cable should increase as $\langle f_b \rangle^{1/2}$. As the membrane becomes more and more leaky, distant points are, electrically speaking, less and less coupled to the soma. Because the dendritic tree contains no active conductances, the electrotonic distance from the soma to a point in the apical bush (about 1 mm away from the soma) is the same in the active and the passive model. Given the square root dependency of L on $\langle f_b \rangle$, this distance, computed as the sum of all branch segments on the path between the location and the soma increases by a factor of 2.5 as $\langle f_b \rangle$ increases from 0 to 2 Hz.

A graphic demonstration of the effect of varying $\langle f_b \rangle$ on the electroanatomy of the cell is given in Fig. 18.6 using the graphical morphoelectronic transform (MET) (see Sec. 3.5.4) of Zador (1993) and Zador, Agmon-Snir, and Segev (1995). Each dendritic compartment is "stretched" or "shrunk" such that its length in the graph is proportional to its electrotonic

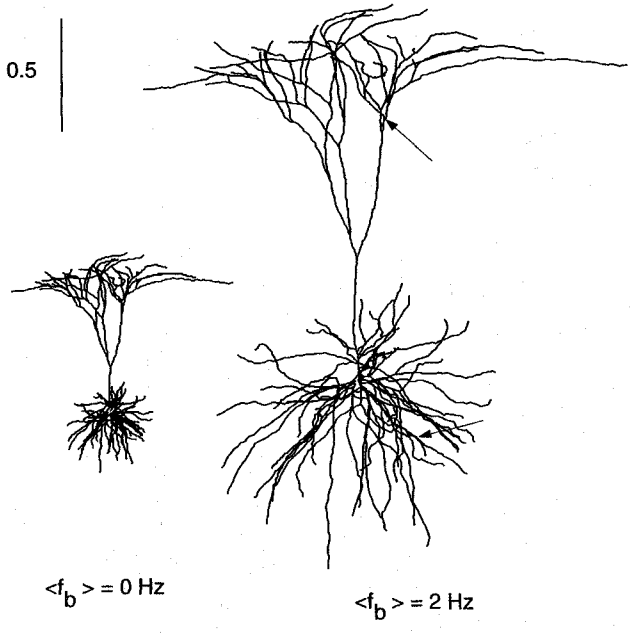

Fig. 18.6 Variable Electroanatomy of Pyramidal Cell Graphic illustration of the change of the electrotonic dimensions of the pyramidal cell with synaptic background activity with the aid of a morphoelectronic transform. The extent of the individual dendrites is proportional to their electrotonic length; the distance of each compartment from the soma is proportional to the electrotonic distance of that point from the soma. In the absence of any background activity—approximating the conditions prevalent in cultured or in slice neurons—the pyramidal cell is very compact. As $\langle f_b \rangle$ is increased to 2 Hz, distal sites on long and thin dendrites are more and more decoupled from the soma. The scale bar corresponds to the distance over which the sustained voltage decays by $e^{0.5}$ in an infinite cable. The arrows point to the location of the apical and basal synapses used in Fig. 18.1. Reprinted by permission from Bernander et al., (1991).

length L_i. L increases from 1.2 to 2.6 for the most distal compartment in layer 1 and from 0.2 to 0.7 for a synapse at the tip of a basal dendrite. That basal dendrites stretch more than apical ones is due to their higher synaptic innervation and the corresponding lower effective values of R_m.

Yet another way to visualize the change in electrotonic properties is to plot the somatic EPSPs evoked by a fast non-NMDA excitatory synapse located either in the distal apical tree, along a basal dendrite, or at the soma (Fig. 18.7). While the amplitude of the somatic and basal EPSPs decrease by a factor of 2 or 3 as $\langle f_b \rangle$ changes from 0 to 5 Hz, the effect on the distal apical synaptic input is much more dramatic. For $\langle f_b \rangle = 5$ Hz, almost no deviation from the somatic resting potential is seen.

18.3.4 Resting Potential

Of the four variables considered here, only E_{eff} depends on the balance of excitatory and inhibitory input (Eq. 18.8). For large values of $\langle f_b \rangle$, V_{soma} depolarizes by close to 10 mV (Fig. 18.4D). This is a consequence of the fact that 80% of the synapses are excitatory and the assumption that the synaptic background activity is the same for excitatory as well as for inhibitory afferents. The somatic potential does not increase indefinitely with $\langle f_b \rangle$, but saturates due to the interaction between the net excitatory and inhibitory synaptic currents and the voltage-dependent potassium currents I_A and I_M, driving the potential to -95 mV (for more details, see Bernander, 1993).

It is known that the resting potential differs significantly between neurons recorded *in vivo* and *in vitro*. Numerous slice studies of pyramidal cells report resting potentials in the range of -84 to -67 mV (with a mean of -74 mV; Thomson, Girdlestone, and West,

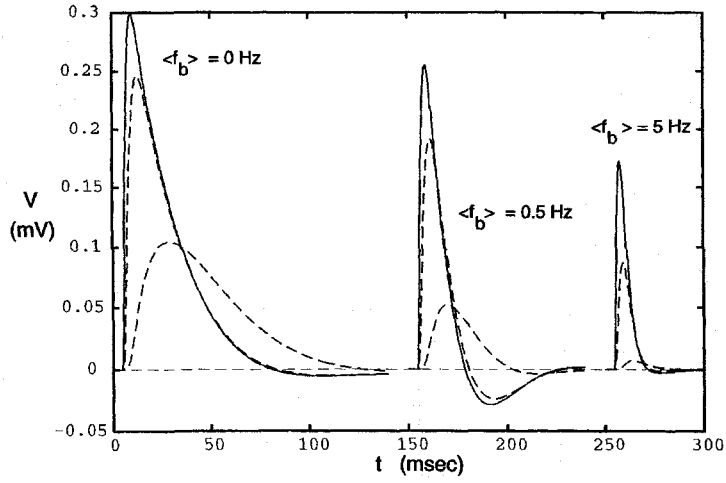

Fig. 18.7 SYNAPTIC INPUT IN THE PRESENCE OF BACKGROUND ACTIVITY Somatic EPSP in response to activation of a single non-NMDA synapse at one of three locations in the pyramidal cell (from top to bottom: soma, basal, and apical tree; see Fig. 18.6) at three different levels of synaptic background activity. The largest EPSPs are obtained under slice conditions ($\langle f_b \rangle = 0$). For 25,000 synaptic events per second ($\langle f_b \rangle = 5$ Hz), the peak somatic, basal, and apical EPSPs are reduced by factors of 1.7, 2.8, and 14.9 relative to their peak values at $\langle f_b \rangle = 0$. The middle set of EPSPs corresponds to the panel of Fig. 18.1B. Notice the much shorter rise and decay times at higher background frequencies. Reprinted in modified form by permission from Bernander (1993).

1988; Mason and Larkman, 1990; Spain, Schwindt, and Crill, 1990; Hirsch and Gilbert, 1991; Mason, Nicoll, and Stratford, 1991), while *in vivo* V_{rest} is usually in the range of -81 to -57 mV (with a mean of -64.5 mV; Bindman and Prince, 1983; Bindman, Meyer, and Prince, 1988; Holmes and Woody, 1989; Pockberger, 1991). Whether this difference is caused primarily by the difference in synaptic background activity remains open.

18.3.5 Functional Implications

The principal effects of modulating the synaptic background activity on the spatio-temporal properties of individual neurons are clear-cut: as $\langle f_b \rangle$ increases from no activity to physiological values in the 5–10 Hz range, input resistance, and space and time constants decrease. Functionally, the cell becomes more and more extended and sensitive to temporal synchrony. This conclusion is not dependent on the numerical details and occurs in simple, analytical cable models (Abbott, 1991; Bernander, 1993) as well as in detailed compartment models of Purkinje (Rapp, Yarom, and Segev, 1992) and pyramidal cells (Bernander et al., 1991). This phenomenon is contingent upon two key assumptions: (1) that the effective membrane resistance in the absence of synaptic background activity is high and (2) that on the order of several thousand (or more) spontaneous synaptic events occur every second. If these conditions are not met, background activity will have either no or only a negligible effect on the spatio-temporal properties of the cell. Note well that these effects would not be observed if synaptic inputs were treated as current inputs.

While it is undoubtedly important to understand the effect of $\langle f_b \rangle$ at the level of an individual cell, a more functionally relevant question is to what extent the spontaneous firing activity is under the control of other brain systems. In particular, to what extent and how fast can neuromodulators up or down regulate $\langle f_b \rangle$ for entire groups of neurons? If they can, the phenomena discussed here could have a number of interesting implications for neuronal information processing strategies.

For instance, in the dark few cells in the visual cortex will be active and the membrane time constant τ_m will be long, enabling the cell to integrate the input over a long time. Conversely, for bright, high contrast visual stimuli, the overall network activity may be much higher, leading to a small value of τ_m and short integration times. This *adaptive gain-control* mechanism is somewhat akin to that used by the network of coupled rods in the retina (Detwiler, Hodgkin, and McNaughton, 1980). As exemplified in Fig. 18.6, larger values of $\langle f_b \rangle$ decouple distal sites from the soma. Because the apical tufts in layers 1 and 2 constitute the dominant target zones for cortico-cortical feedback connections (Friedman, 1983; Rockland, 1994; Salin and Bullier, 1995), a large degree of afferent activity would decouple this feedback by increasing its distance from the soma, thereby making the cell more responsive to direct sensory input arriving on the proximal parts of the apical trunk.

It is obvious that the properties of individual neurons influence the behavior of the embedding neuronal network, such as whether or not it converges to a fixpoint and its convergence time. We have here an instance of the converse, where a collective property of the network—its average activity—modulates the properties of individual members of the network. Particularly intriguing is the fact that the temporal resolution of neurons increases as the mean network activity increases. This illustrates the strong two-way interdependency of the many structural levels of neurobiological hardware, in stark contrast to computer hardware. An intriguing but open question is the issue of stability: under what conditions can a network that modulates the electrical properties of its elements arrive at a stable equilibrium point, that is, how can homeostasis be achieved?

18.4 Relating Synaptic Input to Output Spiking

So far, we have always evaluated the effect of synaptic input to the somatic membrane potential, since it is here—or in the axonal hillock close to the cell body—that the output of the cell—spikes—is generated. But, ultimately, we wish to understand the relationship between synaptic input and the firing activity of the cell.

This is a difficult problem due to the nonstationary nonlinearities at the soma. If EPSPs arrive while the somatic potential hovers just below the spiking threshold, it might be enough to push the potential above threshold, while the arrival of EPSP following an action potential might have a negligible effect on the output frequency. Furthermore, it also makes a difference whether the synapse is activated only once or repeatedly. We will sidestep these problems by adopting the stance we did in the previous sections, that is, we assume that the synaptic inputs are independent of each other and that each individual rate can be replaced by a suitable average (Eq. 18.5) which we assume for simplicity's sake to be directly proportional to the presynaptic firing frequency.

As opposed to conventional cable theory, we will not compute the somatic potential evoked by synaptic input but the current $I_{\text{syn},s}$, flowing longitudinally down the dendrite into the soma. It is this current that will be seen by the spiking mechanism at the cell body and axon hillock and that will ultimately cause the cell to generate axon potentials. Knowledge of $I_{\text{syn},s}$, in conjunction with the f–I curve, allows us to go directly from synaptic input to firing output. We here follow the exposition of Bernander, Douglas, and Koch (1994).

18.4.1 Somatic Current from Distal Synaptic Input

We follow Abbott (1991) in computing the current flowing out of one terminal of a single cable when one or more synapses are activated at the other terminal at $X = L$. (The cable has the electrotonic length $L = \ell/\lambda$ and diameter d.) We can think of the $X = 0$ terminal as being connected to an RC compartment representing the soma. Activating the synapses causes ionic current to flow into the cable and along the transversal intracellular resistivity toward the low-impedance cell body.

Because we are averaging over a fraction of a second or longer we can neglect the capacitive term in our modified cable equation (Eq. 18.12), and—following Eq. 2.2—express the current $I_{\text{syn},s}$ flowing into the soma by the derivative of the voltage along the cable divided by the longitudinal resistance,

$$I_{\text{syn},s} = -\frac{1}{r_a}\frac{dV}{dx}\bigg|_{X=0}. \tag{18.14}$$

The excitatory synapses increase the membrane conductance at $X = L$ by $\overline{g_e}\,\langle f_e\rangle$ (with $\langle f_e\rangle$ the presynaptic firing rate of the excitatory synapses and $\overline{g_e}$ the time-averaged conductance per area; Eq. 18.6) in series with the synaptic reversal potential E_e. In order to compute the current, we need to know the voltage. As in Eq. 2.18, the voltage in this finite cable can be expressed as

$$V(X) = \alpha\cosh(L - X) + \beta\sinh(L - X). \tag{18.15}$$

Solving this requires two boundary conditions. The voltage at the synaptic terminal is given by the usual synaptic equation (Eq. 4.12) as

$$V(L) = \frac{R_{\text{in}}\overline{g_e}\,\langle f_e\rangle\, E}{1 + R_{\text{in}}\overline{g_e}\,\langle f_e\rangle}. \tag{18.16}$$

As argued in the preceding chapter, the spike mechanism at the soma acts as a sort of voltage clamp, preventing the membrane potential from making long-term excursions beyond V_{th}. For the sake of convenience, Abbott (1991) clamps the potential at the $X = 0$ terminal to 0. This also specifies the input resistance R_{in} at the synaptic terminal as the resistance associated with a killed-end terminal (Eq. 2.24),

$$R_{\text{in}} = R_{\infty} \tanh(L) = r_a \lambda \tanh(L) . \tag{18.17}$$

Remembering that the derivative of $\sinh(L - X)$ is $\cosh(L - X)/\lambda$ and that $\sinh^2(x) - \cosh^2(x) = -1$, we arrive at the following expression for the current flowing into the voltage-clamped terminal at $X = 0$,

$$I_{\text{syn},s} = -\frac{\overline{g_e}\,\langle f_e \rangle\, E_e}{\cosh(L) + \lambda r_a \overline{g_e}\,\langle f_e \rangle \sinh(L)} . \tag{18.18}$$

If the input is small relative to the local input resistance, the current is linearly related to the input frequency. As $\langle f_e \rangle$ increases, the local postsynaptic potential starts to saturate, limiting the amount of current that enters through the synapse. Finally, the driving potential $E_e - V(L)$ is close to zero and no amount of presynaptic firing activity will push any additional current through the synapse and toward the other terminal (Fig. 18.8). The limiting current (in the sense that it cannot be exceeded without amplification) at the $X = 0$ terminal becomes

$$I^{\text{sat}}_{\text{syn},s} = -\frac{\pi d^2 E_e}{4\lambda R_i} \frac{1}{\sinh(L)} . \tag{18.19}$$

Two important remarks. The saturation of the net current delivered by the synaptic input to the soma has very little to do with current losses along the cable. If no current leaks across the membrane by postulating $G_{\text{eff}} \to 0$, $I^{\text{sat}}_{\text{syn},s}$ only increases by a factor of $\sinh(L)/L$.

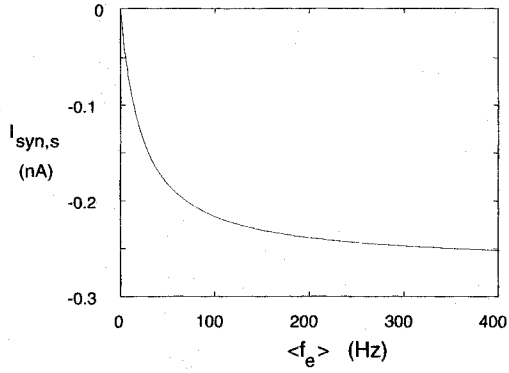

Fig. 18.8 Longitudinal Current in a Single Cable Excitatory synaptic input is applied to one end of the same finite cable (of electrotonic length $L = 1.138$ used in Fig. 18.4), and the other terminal, conceptually corresponding to the soma, is clamped to the resting potential. The longitudinal current $I_{\text{syn},s}$ flowing from the synapses into the $X = 0$ terminal clamped to 0 (Eq. 18.18), is computed as a function of the averaged presynaptic firing rate of the excitatory input $\langle f_e \rangle$. The saturating characteristic has little to do with current leaking out across the membrane. Indeed, preventing any current from leaking across the membrane only increases the maximal current $I^{\text{sat}}_{\text{syn},s}$ by 23%. The culprit is local saturation of the membrane potential at the synaptic terminal. No amount of synaptic input can generate more current $I_{\text{syn},s}$ (unless the membrane contains amplifying currents, as discussed in the following chapter).

Also, $I_{syn,s}$ does *not* correspond to the current that is computed with the aid of the transfer resistances (see the closing comments to Sec. 3.5.3).

18.4.2 Relating f_{out} to f_{in}

The key idea is to assume that the spike generation process at the cell body and axonal hillock can be treated as a stationary nonlinearity whose exact form is given by the discharge curve, that is, by the plot of the output frequency f_{out} against the amplitude of the injected current step (see Figs. 17.10A and 18.10A). It does not matter to this spike triggering mechanism whether the current it sees is injected from a microelectrode or is delivered from a synapse via the dendritic tree. All that is relevant is that a particular current I can be associated to a particular output spiking frequency along the f–I curve. We incorporate the spike frequency adaptation into our consideration by directly making use of the fully adapted f–I curve.

Knowing the relationships between the steady-state input frequency $\langle f_{in} \rangle$ and the somatic current $I_{syn,s}$ (as in Eq. 18.18) on the one hand, and the adapted f–I curve on the other allows us to derive an unique function relating $\langle f_{in} \rangle$ to f_{out},

$$f_{out}(\langle f_{in} \rangle) = f_{out}(I_{syn,s}(\langle f_{in} \rangle)) \tag{18.20}$$

(see Fig. 18.9).

Bernander Douglas, and Koch (1994) use this procedure to derive the input-output relationship for the layer 5 pyramidal cell. $I_{syn,s}$ is estimated on the basis of two different

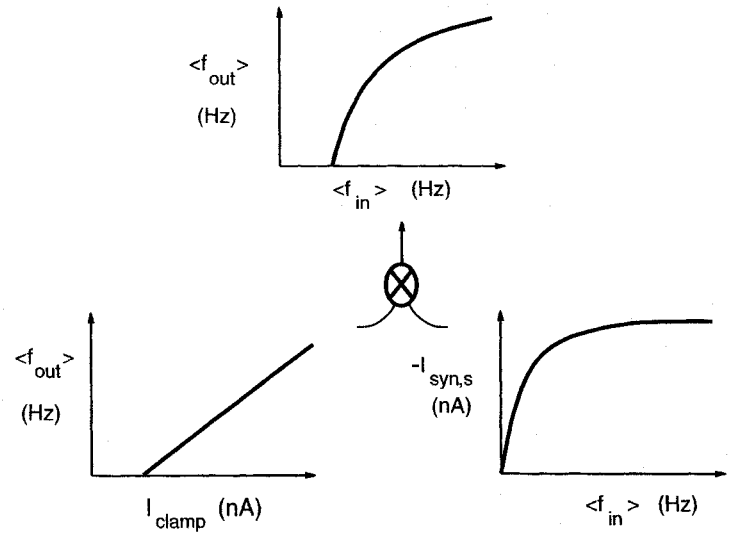

Fig. 18.9 Complete Measure of Synaptic Efficiency Schematic illustrating the procedure linking the time-averaged presynaptic input frequency $\langle f_{in} \rangle$ to the adapted output frequency f_{out} of the cell via Eq. 18.20. It requires knowledge of the relationship between the presynaptic firing frequency $\langle f_{in} \rangle$ and the current flowing from the synapse into the soma $I_{syn,s}$ (lower right) and the discharge curve f–I (lower left; here a linear function, although this is not necessary). The former function accounts for properties of the synapses and the dendritic tree, the latter for the somatic spike-generating properties. The resulting function $f_{out}(\langle f_{in} \rangle)$ accounts for the synaptic conductance input, synaptic saturation, and active, voltage-dependent membrane conductances. The intermediate variable is current, and not—as in the standard cable equation—voltage. Reprinted by permission from Bernander (1993).

methods. Knowledge of $I_{syn,s}$ requires that the somatic membrane potential $V_m(t)$ be known. In the derivation of Eq. 18.18 it was assumed that $V(0)$ was clamped to 0. When the cell spikes, this is patently wrong. Since the considerations of this section are predicated on using a time-averaged input frequency, why not use the time-averaged membrane potential $\langle V_m \rangle$ of Eq. 17.12? As we discussed in Sec. 17.5.2, this quantity changes only little for large swings in spiking activity. Indeed, the cumulative action of the voltage-dependent somatic currents is to clamp, albeit imperfectly, $\langle V_m \rangle$ to around -50 mV, corresponding to moderate values of f_{out} in the 50-Hz range. Bernander and colleagues (1994) compute the clamp current required to hold the somatic potential to -50 mV for a fixed synaptic input and subtract the clamp current needed to hold V_{soma} to -50 mV in the absence of any synaptic input. This method was also used experimentally to measure $I_{syn,s}$ in response to a constant synaptic input in α motoneurons (Powers, Tobinson, and Konodi, 1992). In the second method, $I_{syn,s}$ is computed directly (without voltage clamping the soma) as the current flowing between the first segment of the apical tree and the soma. Both methods give identical results.

As can be seen in Fig. 18.10B and C, when 500 excitatory non-NMDA synapses are either placed directly onto the cell body or spread throughout the basal dendrites (almost exclusively restricted to layer 5), $I_{syn,s}$ is linear in $\langle f_{in} \rangle$ over the range of interest. Saturation only becomes evident as the same 500 synapses are moved to layer 4 or to the more distal parts of the apical tree in superficial layers. When all inputs are confined to the superficial layers 1, 2, and 3, $I_{syn,s}$ is at most 0.65 nA. The saturation effect is even more extreme when synaptic input is restricted to the top two layers 1 and 2. Even if all 500 synapses are activated at an unphysiological 500 Hz, at most 0.25 nA of current reaches the soma (and this across an apical dendrite that has an unusually thick trunk of about 4.4 μm). This strong saturation is due to the fact that the distal input is associated with high input impedances, driving the local potential quickly to the synaptic reversal potential. No amount of further synaptic input can increase the synaptic current. Saturation would *not* occur if synaptic input were treated as a pure current. As in the case of the single cable, the minuscule current contributed from distal sites is not due to leakage through the membrane as the current spreads to the soma. Indeed, eliminating leakage by setting $R_m \rightarrow \infty$ causes the maximal current to increase by only 2% above base level.

In the last panel in Fig. 18.10, these somatic currents are translated on the basis of the adapted discharge curve (Fig. 18.10A) into an output firing rate. Because of the current threshold, synaptic input that delivers less than $I_{th} = 0.29$ nA current to the soma will be cut off. For instance, by itself, input to layers 1 and 2 will not lead to any maintained spike discharge, no matter how big the synapses and how vigorous their presynaptic activity, while the addition of synapses to layer 3 leads to a very weak discharge. And yet, these dendrites make up 26% of the surface area of the tree. Above threshold, the adapted f–I curve is reasonably linear (Eq. 17.10), with a slope of 50 spikes per second per nanoampere of current, leading to linear input-output relationships for synaptic input to the soma or the basal dendrites (contributing 62% of the total membrane area of the neuron). As a sanity check, Bernander and colleagues explicitly computed the adapted firing rate as a function of the input and superimposed this onto Fig. 18.10D, with little difference.

18.4.3 Functional Considerations

The standard measures of the synaptic efficiency of cable theory are voltage or charge attenuation (see Chap. 3). The advantage of using the total current $I_{syn,s}$ flowing from one or more synapses into the soma (Powers, Tobinson, and Konodi, 1992; Bernander, Douglas,

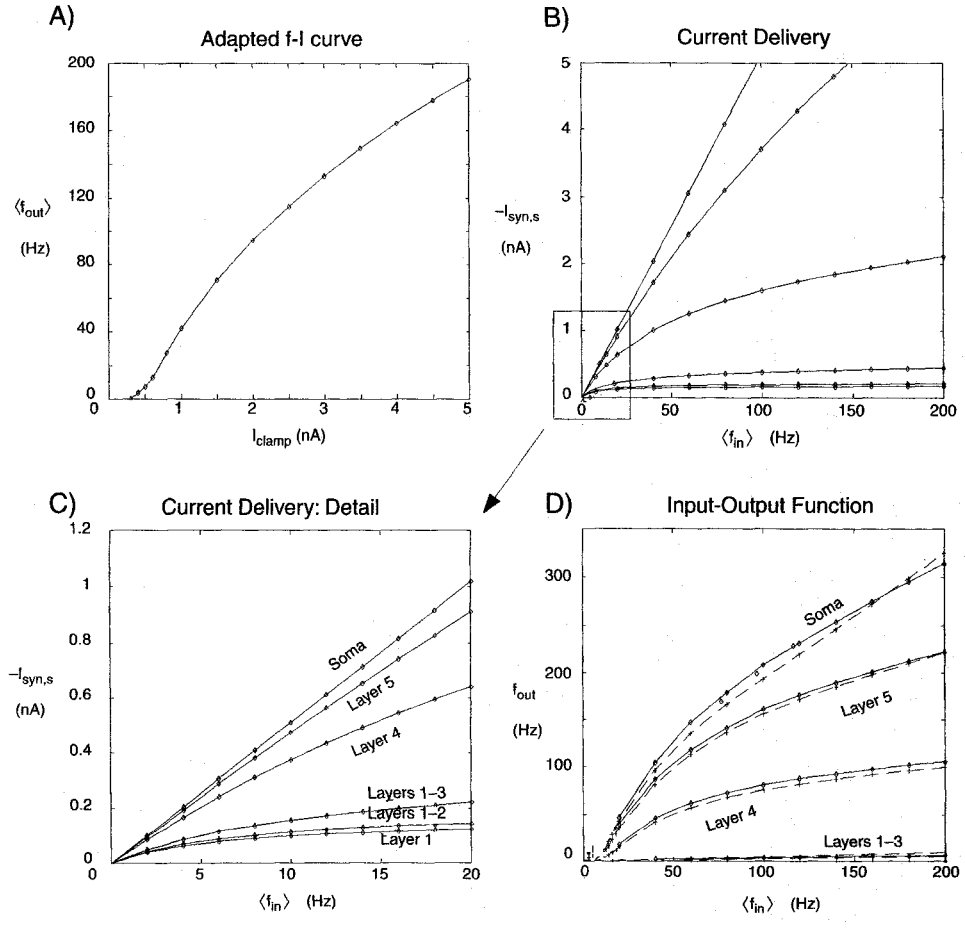

Fig. 18.10 Relating Synaptic Input to the Firing Frequency Characterizing the input-output behavior of the layer 5 pyramidal cell using the procedure illustrated in Fig. 18.9. **(A)** For ease of comparison, its adapted f–I discharge curve. **(B)**, and **(C)** The input, 500 excitatory non-NMDA synapses, is placed onto the soma or the portion of the dendrites running through a specific cortical layer. The postsynaptic conductance increase is related linearly to the presynaptic firing rate $\langle f_{in} \rangle$. These synapses cause the current $I_{syn,s}$ to flow into the soma. The different curves correspond to synaptic placement (from top to bottom) onto the soma, layer 5, layer 4, layers 1 to 3, layers 1 and 2, and layer 1 only. Similar to Eq. 18.18, dendritic saturation causes the distal input to saturate. **(D)** $I_{syn,s}(\langle f_{in} \rangle)$ is passed through the cell's discharge curve to predict the relationship between $\langle f_{in} \rangle$ and f_{out} (dashed curves). Computing this function by direct simulation (solid curves) leads to very similar results. Because $I_{syn,s}$ for synaptic input from layers 1 and 2 is less than I_{th} (about 0.295 nA), these synapses—assuming a passive dendritic membrane—cannot contribute by themselves to the maintained discharge. Experimentally, it is known that synaptic input to the apical tuft *can* trigger spikes in the cell body far away (Cauller and Connors, 1992, 1994). This argues for the existence of dendritic voltage-dependent currents that counteract saturation and amplify $I_{syn,s}$ (see the following chapter).

and Koch, 1994) is that this measure includes the effects of synaptic nonlinearities and interactions among different inputs. Furthermore, as we will show in the following chapter, $I_{syn,s}$ can also be derived in the presence of voltage-dependent dendritic conductances, when all other measures break down. If two synaptic sites are well separated such that the voltage in one does not readily influence the voltage at the other location (for instance, input

into the basal dendrites coupled with input to the apical tuft), the total current at the soma will be the sum of the individual $I_{syn,s}$ components.

Computing the current flowing into the soma is relatively straightforward as long as V_{soma} is fixed (see the derivation of Eq. 18.18). However, this is not the case if $I_{syn,s}$ is above I_{th}, leading to spike generation. Under these conditions, $V_{soma}(t)$ moves on a stable limit cycle, making it difficult to characterize synaptic input using a single voltage measure, such as the peak somatic EPSP. Yet the method advocated here works despite these complexities (as witnessed by the close match in Fig. 18.10D between the predicted input-output curves and the actual ones) by making use of the time-averaged somatic potential $\langle V_m \rangle$ (Eq. 17.12). Its key assumption is that the system is in equilibrium, that is, the input can be characterized by an averaged input rate and the postsynaptic firing rate has adapted (typically within 100 msec). In a more sophisticated model, adaptation could be incorporated by making the f–I curve time dependent. Likewise, short-term synaptic facilitation and depression could also be dealt with.

As applied to the pyramidal cell, the main conclusion is that in the absence of voltage-dependent dendritic conductances distal synaptic input by itself can only deliver a very limited amount of current to the soma. In conjunction with other synaptic input, such as to the basal dendrites, distal input could increase the maintained rate by about 12 spikes per second.

In the neocortex, much of the synaptic input into layer 1 originates in higher cortical processing stages (Friedman, 1983; Rockland, 1994; Salin and Bullier, 1995). In the absence of amplifying dendritic conductances, cortico-cortical feedback could only weakly modulate the firing of the pyramidal cell. Yet Cauller and Connors (1992, 1994) have provided experimental evidence that synaptic input onto the layer 1 portion of layer 5 pyramidal cells in the somatosensory cortex can evoke action potentials. This, together with the evidence reviewed in the following chapter, argues that voltage-dependent conductances in the dendritic tree serve to amplify distal inputs.

18.5 Shunting Inhibition Acts Linearly

Inhibitory synaptic input with a reversal potential close or equal to the local resting potential, *shunting inhibition*, first mentioned toward the end of Chap. 1 and treated in considerable detail in Sec. 5.1.4, acts nonlinearly, akin to a division (Blomfield, 1974). This type of nonlinear operation has been proposed to be the crucial biophysical mechanism underlying retinal direction selectivity (Torre and Poggio, 1978; Koch, Poggio, and Torre, 1982). More recently, both Carandini and Heeger (1994) and Nelson (1994) have made shunting inhibition, activated by a recurrent feedback loop, the centerpiece of a gain normalization circuit in the visual cortex (Fig. 1.11) and in electric fish. However, none of these studies considered the effect that the spiking mechanism has on the divisive action of shunting inhibition. When this is done, a surprising conclusion emerges (Holt and Koch, 1997).

For the sake of clarity, let us first consider shunting inhibition to the leaky integrate-and-fire model of Eq. 14.7. Using our standard synaptic averaging technique, shunting inhibition can be mimicked by decreasing the leak resistance appropriately, with the new value given by

$$g_{leak} = g_l + \frac{1}{R} \tag{18.21}$$

where R is the value of the resistance in the absence of any input. The result can be inspected in Fig. 18.11A. Increasing g_i shifts the curve toward the right, with the slopes remaining constant, contrary to what one would expect based on models that only treat the subthreshold domain (as in Fig. 1.10 and throughout Chap. 5). Adding a refractory period and adaptation does not change this conclusion. The same is also true if one considers the much more realistic scenario of $GABA_A$ inhibitory receptors, with a reversal potential of -70 mV, which are distributed at and around the soma. As in the previous section, the total amount of inhibition is postulated to be proportional to the presynaptic firing frequency (Eq. 18.5). Holt and Koch (1997) compute the average f_{out}–f_{in} curve by varying the input frequency of the excitatory voltage-independent synaptic input distributed throughout the tree. Changing the amount of inhibition leads to a clear shift in the curves with little effect on the slopes (Fig. 18.11B).

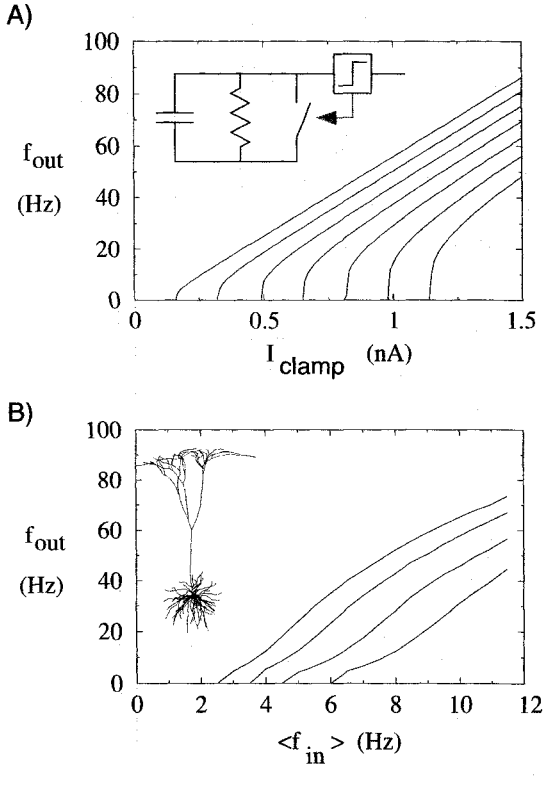

Fig. 18.11 SHUNTING INHIBITION AND SPIKING Shunting inhibition has a subtractive rather than a divisive effect on firing rates. This is demonstrated in two different single-cell models. **(A)** Discharge curves for a leaky integrate-and-fire unit with different values for the leak conductance $g_{leak} = g_i + 1/R$ (for $R = 62.5M\Omega$). g_i is the amplitude of the inhibitory conductance change whose reversal potential is equal to the unit's resting potential (here zero). Varying g_{leak} in steps of 10 nS from 10 to 70 nS (from left to right) shifts the curve, rather than changing the slope of the discharge curve. **(B)** The same observation is made in the pyramidal cell model, with $GABA_A$ inhibition around the soma and excitatory voltage-independent input distributed throughout the cell. The fully adapted postsynaptic firing rate is plotted as a function of the average input frequency to the excitatory synapses for four different settings of presynaptic firing rates to the $GABA_A$ synapses (0.5, 2, 4, and 6 Hz, left to right). Reprinted by permission from Holt and Koch (1997).

This effect is most easily understood in the integrate-and-fire model. In the absence of any spiking threshold, the membrane potential in response to a synaptic input current of the shunting type

$$I_{\text{syn}} = g_i(V - E_i) = g_i V \tag{18.22}$$

rises until

$$V = \frac{I_{\text{syn}}}{g_{\text{leak}}} \tag{18.23}$$

(Fig. 18.12). Under these conditions, the steady-state leak current is proportional to the input current and the divisive effect is observed (Eq. 1.35). However, in the integrator model, V never rises above the spiking threshold V_{th}. No matter how large the input current, the leak current can never be larger than $V_{\text{th}} g_{\text{leak}}$. The effect of the leak conductance can be replaced by a current whose amplitude is equal to the time-average value of the current through the leak conductance: $\langle I_{\text{leak}} \rangle = g_{\text{leak}} \langle V \rangle$. This trick reduces the leaky integrate-and-fire unit to a perfect integrator. The cell will still fire at exactly the same rate because the same charge $\int (I_{\text{syn}} - I_{\text{leak}}) dt$ is deposited on the capacitor in the same time interval, although for the leaky integrator the deposition rate is not constant.

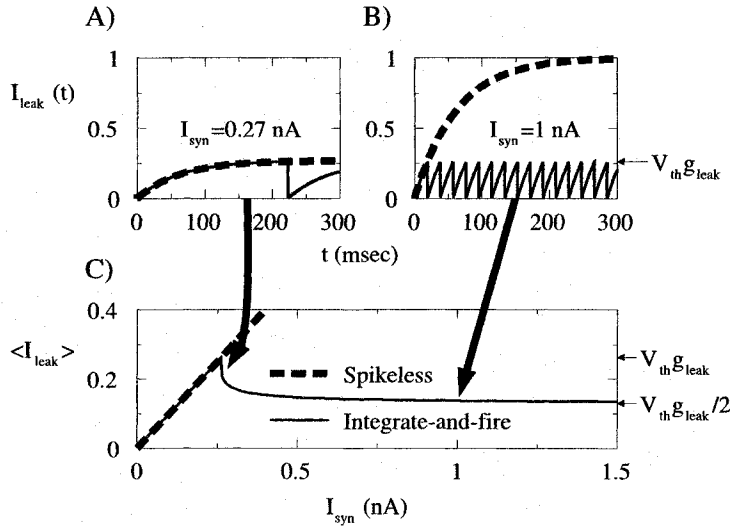

Fig. 18.12 Why Shunting Inhibition Has a Subtractive Effect **(A)** Time-dependent current across the leak conductance I_{leak} (in nA and equal to $V(t)g_{\text{leak}}$) in response to a constant 0.5-nA current injected into a leaky integrate-and-fire unit with (solid line) and without (dashed line) a voltage threshold V_{th}. The sharp drop in I_{leak} occurs when the cell fires, since the voltage is reset. **(B)** Same for 1-nA current. Note that I_{leak} in the presence of a voltage threshold has a maximum value well below I_{leak} in the absence of a voltage threshold. **(C)** Time-averaged leak current $\langle I_{\text{leak}} \rangle$ (in nanoamperes) as a function of input current, computed from Eqs. 18.24 and 18.25. Below threshold, the spikeless model and the integrate-and-fire model have the same $\langle I_{\text{leak}} \rangle$, but above threshold $\langle I_{\text{leak}} \rangle$ is reduced considerably. For I_{syn} just greater than threshold, the cell spends most of its time with $V \approx V_{\text{th}}$, so $\langle I_{\text{leak}} \rangle$ is high. For high I_{syn}, the voltage increases approximately linearly with time and V has a sawtooth waveform, as shown in **B**. This means that $\langle I_{\text{leak}} \rangle = (\max I_{\text{leak}})/2 = V_{\text{th}} g_{\text{leak}}/2$. Reprinted by permission from Holt and Koch (1997).

For a constant input that is just above threshold, $\langle V \rangle$ will be close to V_{th} and $\langle I_{leak} \rangle$ will be large. For larger synaptic input currents, the time-averaged membrane potential becomes smaller and smaller (since V has to charge up from the reset point) and, therefore, the time-averaged leak current *decreases* for increasing inputs (compare Fig. 18.12A and B). It can be shown that

$$\langle I_{leak} \rangle = I_{syn} \tag{18.24}$$

if $I_{syn} < V_{th} g_{leak}$. Otherwise

$$\langle I_{leak} \rangle = V_{th} g_{leak} \left(\frac{I_{syn}}{V_{th} g_{leak}} + \frac{1}{\ln\left(1 - V_{th} g_{leak} / I_{syn}\right)} \right) . \tag{18.25}$$

For even quite moderate levels of I_{syn} just above $V_{th} g_{leak}$, the lower expression is approximately equal to $g_{leak} V_{th}/2$, independent of I_{syn} (Fig. 18.12C), and the leak conductance can be replaced—to a good first approximation—by a constant offset current. The discharge curve for the resulting perfect integrate-and-fire neuron is

$$f_{out} = \frac{I_{syn} - \langle I_{leak} \rangle}{C V_{th}} = \frac{I_{syn}}{C V_{th}} - \frac{g_{leak}}{2C} . \tag{18.26}$$

The same mechanism explains the result for the compartmental models. Here, the voltage does rise above the firing threshold but because the spike repolarization currents are large, any current from synapses flowing into the soma is ignored during the brief spike. The time-averaged somatic membrane potential (Fig. 17.10B) always remains close to V_{th}.

Two caveats. These results hold because inhibition is at or very close to the soma. For more distal inhibition, as for instance in retinal ganglion cells, the local potential at the inhibitory synapse it not limited by V_{th} and shunting inhibition will work in a more divisive mode. Yet for such distal sites, its effect on the spike triggering zone far away will be small. The results discussed here assume that the synaptic input changes slowly. It is at present unclear what the effect of very high, but transient input frequencies to the inhibitory synapses will be.

18.6 Recapitulation

The past few pages treated synaptic input arriving at the passive dendritic tree of a spiking cell. Only the cell body is assumed to contain voltage-dependent membrane conductances. We first discussed unitary EPSPs and EPSCs, concluding that the former can be used to predict quite well the voltage threshold V_{th} of the cell. We then investigated the exact relationship between the temporal jitter in a normally distributed set of synapses σ_{in} and the jitter in the output spike σ_{out}. Surprisingly, we discovered that $\sigma_{out} \propto \sigma_{in}$, with the constant of proportionality being much less than unity. Once again (e.g., Chap. 14) for strong synaptic input (that is, in the above threshold domain), the passive membrane time constant plays only a minor role in determining the temporal behavior of the cell. This has important implications, in particular for the faithful conservation of timing relationships across many layers of neurons (Abeles, 1990; Marsalek, Koch, and Maunsell, 1997).

For the remainder of the chapter we assume that synaptic input is not correlated at a fine time scale and that, indeed, we can define an average input frequency $\langle f \rangle$. This allows us to treat massive synaptic input in three separate cases.

Neurons receive between 10^3 and 10^5 synapses onto their dendritic tree from other neurons that fire spontaneously between 1 to 10 or more spikes per second in the behaving animal. This massive synaptic background activity has several effects on the spatio-temporal behavior of the cell. As this background firing rate goes up, the electrotonic dimensions of the cell increase (that is, distal synaptic input becomes more decoupled) and the input resistance and time constant decrease by one or more orders of magnitude. This implies, among other things, that the cell becomes more sensitive to temporal coincidences as the overall network activity increases. Given the rapid changes in firing activity in large parts of the brain, as assessed by EEG and other macroscopic techniques recording large-scale brain activity, this implies that the collective behavior of the network can directly influence the spatio-temporal integrative properties of individual neurons.

We also described a method that characterizes the efficiency of massive synaptic input, involving the current $I_{syn,s}$ that is delivered by synaptic input to the soma. Deriving $I_{syn,s}$ for synaptic input to a particular spatial region in the tree firing at a frequency $\langle f_{in} \rangle$ has the major advantage that the resultant function can be combined with the f–I curve measured at the soma to yield a complete relationship between the sustained presynaptic input firing frequency $\langle f_{in} \rangle$ and the adapted output firing rate f_{out}.

When this method is applied to study synaptic input into the distal part of the apical tree of a pyramidal cell, it is seen that the current from these sites (1) saturates already at very small presynaptic firing rates and (2) influences the maintained firing rate only marginally. This saturation is only to a very minor extent caused by current leaking across the membrane between the synaptic site and the soma. As we will see in the next chapter, introducing voltage-dependent currents into the dendrite can both prevent saturation and amplify these small currents, effectively turning the apical tree into a better "wire."

Finally, we reexamined the effect of shunting inhibition. While it acts in a divisive manner in subthreshold cable models, it behaves in a linear, subtractive manner when spiking is accounted for. This is due to the fact that the average somatic membrane potential does not exceed the voltage threshold, limiting the maximal inhibitory current. Thus, at least for models where inhibition acts in a maintained manner at or close to the cell body, shunting inhibition does not implement a divisive normalization operation as postulated by many.

However, at the next level of organization, the small recurrently connected network, linear inhibition can act again in a divisive manner (Douglas et al., 1995). We conclude with the observation that a biophysical mechanism that implements one type of operation in the subthreshold domain might implement a quite different one in the suprathreshold domain. The morale is that it is dangerous in neurobiology to study any one mechanism at only a single, isolated level of complexity. Phenomena at multiple levels, such as ionic channel, synapse, dendrite, neuron, small network, and so on, interact in highly nonlinear and nonintuitive ways. This is, of course, a characteristic of any evolved systems and makes them so interesting.

19

VOLTAGE-DEPENDENT EVENTS IN THE DENDRITIC TREE

So far, we worked under the convenient fiction that active, voltage-dependent membrane conductances are confined to the spike initiation zone at or close to the cell body and that the dendritic tree is essentially passive. Under the influence of one-dimensional passive cable theory, as refined by Rall and his school (Chaps. 2 and 3), the passive model of dendritic integration of synaptic inputs has become dominant and is taught in all the textbooks. Paradoxically, from the earliest days of intracellular recordings from the fat dendrites of spinal cord motoneurons with the aid of glass microelectrodes, active dendritic responses had been witnessed (Brock, Coombs, and Eccles, 1952; Eccles, Libet, and Young, 1958). Today, there exists overwhelming evidence for a host of voltage-dependent sodium and calcium-conductances in the dendritic tree. In the following section we summarize the experimental evidence and discuss current biophysical modeling efforts focusing on the question of the existence and genesis of fast all-or-none electrical events in the dendrites. We then turn toward possible functional roles of active dendritic processing.

One word of advice. It has been argued that linear cable theory as applied to dendrites and taught in the first chapters of this book is irrelevant in the face of all this evidence for active processing and can be relegated to the dustbin. However, this would be a mistake. Under many physiological conditions these nonlinearities will not be relevant. Even if they are, the resistive and capacitive cable properties of the dendrites profoundly influence the initiation and propagation of dendritic action potentials and other active phenomena. Thus, for a complete understanding of the events in active dendritic trees we need to be thoroughly versed in cable theory.

19.1 Experimental Evidence for Voltage-Dependent Dendritic Membrane Conductances

The issue of dendritic all-or-none electrical events must be seen as separate from the broader question of the existence and nature of active, that is, voltage-dependent, membrane conductances in the dendritic tree.